Biomass and Bioenergy 193 (2025) 107523

Contents lists available at ScienceDirect

Biomass and Bioenergy

journal homepage: www.elsevier.com/locate/biombioe

High performance metal-free N/S-doped biochars towards oxygen reduction reaction

Renata Matos [a], António J.S. Fernandes [b], Victor K. Abdelkader-Fernández [c], Andreia F. Peixoto [a], Diana M. Fernandes [a,*]

[a] LAQV/REQUIMTE, Departamento de Química e Bioquímica, Faculdade de Ciências da Universidade do Porto, Rua do Campo Alegre s/n, 4169-007, Porto, Portugal
[b] Instituto de Nanoestruturas, Nanomodelação e Nanofabricação (I3N), Departamento de Física, Universidade de Aveiro, Campus Universitário de Santiago, 3810-193, Aveiro, Portugal
[c] Departamento de Química Inorgánica, Facultad de Ciencias, Universidad de Granada, Granada, 18071, Spain

ARTICLE INFO

Keywords:
Doped carbon
Biochars
Shrimp shells
Oxygen reduction
Electrocatalysis

ABSTRACT

The lack of cost-effective electrocatalysts towards oxygen reduction reaction is hindering the large-scale application of promising energy conversion technologies, such as fuel cells or metal-air batteries. In this context, metal free N and S doped carbon materials have been successfully applied to oxygen reduction reaction (ORR) electrocatalysis. Heteroatom doped biochars, in particular, represent a cost-effective and sustainable replacement to Pt-based electrocatalysts. Herein, we developed several N-doped or N and S co-doped biochars, using shrimp shells as biomass feedstock. Four dopants containing different N/S ratios (N_6, SN_6, S_3N_3 and S_3N_2) were used in order to optimize the ORR performance in alkaline medium. Doping with S_3N_3 revealed to be more promising, as the resulting electrocatalyst, S_3N_3-CC, obtained the most positive onset potential (E_{onset}), higher diffusion limiting current density (j_L) and number of electrons transferred per oxygen molecule (n_{O2}) closer to 4. Moreover, this biochar showed excellent stability over 15 h of continuous use. The performance of S_3N_3-CC was mainly explained by a high content of pyridinic and graphitic N, a high ratio between pyridinic and pyrrolic N, the introduction of thiophenic S and an optimized N/S ratio.

It delivers sustainable and cost-effective metal-free carbon electrocatalysts and promotes the valorization of a common waste usually discarded in landfills/ocean.

1. Introduction

Fuel cells and metal-air batteries represent one of the most promising alternatives to fossil fuel combustion [1,2]. These electrochemical energy conversion devices rely on several electrochemical reactions, such

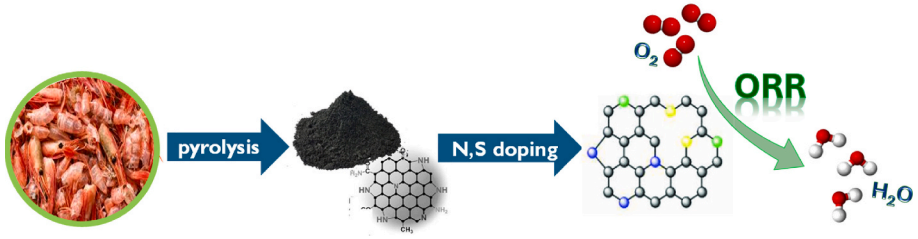

* Corresponding author.
E-mail address: diana.fernandes@fc.up.pt (D.M. Fernandes).

https://doi.org/10.1016/j.biombioe.2024.107523
Received 28 October 2024; Received in revised form 25 November 2024; Accepted 28 November 2024
Available online 5 December 2024

as oxygen reduction reaction (ORR), oxygen evolution reaction (OER), hydrogen oxidation reaction (HOR) or hydrogen evolution reaction (HER) [3]. Unfortunately, all these reactions, including ORR, suffer from large overpotentials and sluggish kinetics, hindering the large-scale application of fuel cells and metal-air batteries [3,4]. Moreover, ORR is catalyzed preferentially by Pt-based electrocatalysts, whose natural rarity and high cost further limit the use of these technologies [5,6].

Lately, heteroatom doped carbon materials have emerged as potential replacements for Pt-based ORR catalysts due to their promising electrochemical properties, excellent stability and lower production cost [7,8]. Heteroatom doping is known to led to enhanced ORR performance: nitrogen [5,9], sulfur [8,10], phosphorous [6,11], fluorine [12,13] and boron [14,15] doped carbon materials have been successfully applied on ORR in the last decades. Depending on the heteroatom doped, it is possible to tune the charge and spin density distribution over the carbon material, creating charged sites with higher affinity to O_2 adsorption and ORR [10,16]. For instance, the introduction of nitrogen atoms, with higher electronegativity than carbon, generates a positive charge density on adjacent carbon atoms [17]. On the other hand, sulfur and carbon have similar electronegativity, and so the ORR performance of S-doped carbon materials is not attributed to charge density redistribution but to polarization of the spin distribution along S-C bonds, usually locate at defects or edge positions [10,16]. Co-doping with nitrogen and sulfur generally leads to enhanced ORR activity compared to single nitrogen or sulfur doping, due to a synergistic effect [18,19]. Nevertheless, it is crucial to control the species of nitrogen and sulfur introduced, as well as the ratio between both heteroatoms, to insure the higher electrocatalytic activity [16].

Biochars are a new class of carbon materials, obtained from the thermochemical conversion of biomass under inert atmosphere or low oxygen conditions [20]. As they are produced from renewable sources, and usually by simple procedures without use of dangerous reactants, biochars are considered more sustainable than conventional carbon materials (e.g. graphene, carbon nanotubes or activated carbon) derived from petrochemical resources [21]. Moreover, biochars may retain some of the heteroatoms originally present in the biomass feedstock [21,22]. Shrimp shells, for instance, are excellent biomass sources as they present a very advantageous chemical composition, containing a large amount of N (under chitin form), as well as lower amounts of S and P [23,24]. Moreover, shrimp shells also contain large contents of $CaCO_3$, which promotes porosity formation by acting as a self-template during biochar preparation [24,25]. Finally, the aspect of circularity should be considered: shrimp shells are a byproduct of the seafood industry and are usually discard in landfills or on the ocean, leading to environmental problems [26,27]. Hence, the valorization of this residue is critical.

Herein, we prepared N-doped or N and S co-doped biochars, derived from shrimp shells, *via* a solventless ball milling approach. Four different heteroatom sources, containing distinct N/S ratios (N_6, SN_6, S_3N_3 and S_3N_2), were used in order to evaluate their effect in ORR performance. The biochar doped with S_3N_3 (S_3N_3-CC) achieved the most promising electrocatalytic results, showing similar n_{O2} to the state-of-the-art Pt/C and excellent stability over 15 h, also obtaining the most positive E_{onset} and higher j_L from the prepared electrocatalysts. While S_3N_3-CC still underperformed the state-of-the-art Pt/C in some parameters, the present work represents a significant advance for the development of more sustainable and cost-effective metal free carbon electrocatalysts, while also promoting the valorization of a common waste.

2. Experimental

2.1. Materials and chemicals

Hydrochloric acid (37 %, Fluka), melamine (N_6, 99 %, Alfa Aesar), 1,3,5-triazine-2,4,6-trithiol (S_3N_3, Sigma-Aldrich), 2-5-dimercapto-1,3,4-thiadiazole (S_3N_2, Sigma-Aldrich), 4-amino-3-hydrazino-5-mercapto-1,2,4-triazole (SN_6, Sigma-Aldrich), dimethylformamide (99.5 %, Sigma-Aldrich), Nafion 117 (5 wt% in lower aliphatic alcohols, Aldrich), potassium hydroxide (99.99 %, Sigma-Aldrich), platinum nominally 20 % on carbon black (Pt/C 20 wt%, HiSPEC® 3000, Alfa Aesar) were used as received. Shrimp shells were obtained from Mar Cabo – Produtos Congelados Lda and grounded to fine powder before utilization. Ultrapure water (resistivity 18.2 MΩ cm at 25 °C, Interlab) was used in all electrochemical analysis; deionized (DI) water was used during the catalysts preparation.

2.2. Catalysts preparation

2.2.1. Preparation of CC

Shrimp shell-derived biochar (denoted as CC from the Portuguese translation of shrimp shells, *casca de camarão*) was prepared through a simple procedure. Powdery shrimp shells were pyrolyzed under N_2 atmosphere (100 mL min^{-1}), at 900 °C (heating rate of 10 °C min^{-1}), for 2 h, in a horizontal tubular furnace. Then, the resulting material was submitted to an acid treatment at 80 °C in a 2 mol dm^{-3} HCl solution, under reflux, for 4 h. After cooling, the biochar was filtrated, washed several times with DI water until reaching neutral pH and dried overnight at 80 °C and 100 mbar in a glass oven.

2.2.2. Preparation of heteroatom doped CC

The procedure for heteroatom doping was adopted from Ref. [28]. Briefly, CC and one of the heteroatom precursors (N_6, S_3N_3, S_3N_2 or S_6N) were mixed together *via* ball milling (Retsch), in a mass ratio of 50:50, using ≈ 100 balls ZrO balls with diameter of 2 mm, at 15 s^{-1} for 5 h. Then, the mixture was pyrolyzed at 800 °C for 1 h, with a heating rate of 5 °C min^{-1}, under N_2 flow (100 mL min^{-1}). The resulting materials doped with N_6, S_3N_3, S_3N_2 and S_6N were denoted N_6-CC, S_3N_3-CC, S_3N_2-CC and S_6N-CC, respectively.

2.3. Characterization techniques

X-ray photoelectron spectroscopy (XPS) analyses were performed on Kratos Axis Ultra HSA spectrometer with monochromatized Al Kα radiation (1486.7 eV) operating at 15 kV (90 W), at Centro de Materiais da Universidade do Porto (CEMUP), Portugal. The samples were pressed into pellets before the measurements. The binding energies were calibrated using the C 1s peak at 284.6 eV as internal reference. The CasaXPS software was used to deconvolute the XPS spectra, employing a non-linear least square fitting routine after a Shirley-type background subtraction. Surface atomic percentages were calculated from the corresponding peak areas upon spectra deconvolution and using the sensitivity factors provided by the manufacturer.

Micro-Raman analyses were performed in the backscattering configuration on a Jobin Yvon HR800 instrument (Horiba, Japan), using a 600 lines/mm grating and the 532 nm laser line from a Nd:YAG DPSS laser (Ventus, Laser Quantum, U.K.). A 100 × objective (spot size < 2 μm, numeric aperture = 0.9, Olympus, Japan) was used to focus the laser light onto the sample and to collect the backscattered Raman radiation to be detected by a Peltier cooled (223 K) CCD sensor. The spectrometer was operated in the confocal mode, setting the iris to 300 μm. The analyses were conducted at Centro de Investigação em Materiais Cerâmicos e Compósitos – CICECO – Universidade de Aveiro (Aveiro, Portugal). Raman spectra were fitted using LabSpec 5.25.15 software, by applying Gaussian-Lorentzian functions after baseline subtraction.

Scanning electron microscopy/energy dispersive spectroscopy (SEM/EDS) results were obtained at CEMUP on high-resolution scanning electron microscope with X-ray microanalysis and backscattered electron diffraction pattern analysis (FEI Quanta 400 FEG ESEM/EDAX Genesis X4M), at 15 kV.

CHNS analyses were performed at Unidad de Análisis Instrumental, Área de Infraestruturas de Investigación of Universidade de Compostela, Lugo, Spain, using a LECO CHNS-932 equipment.

Powder X-ray diffraction (XRD) analyses of the N,S co-doped

biochars were conducted at Centro de Tecnologia Mecânica e Automação (TEMA), Universidade de Aveiro, Aveiro, Portugal using a Rigaku SmartLabSe diffractometer (Cu Kα radiation – 1.5406 Å, 40 kV, 30 mA); the diffractograms were collected in the range $10° < 2\theta < 80°$, with a scan speed of 3° min^{-1} and a step of 0.02°. XRD results of CC and N-CC were collected at Inorganic Chemistry Department, Science Faculty, University of Granada, Granada, Spain, using a Bruker D2 PHASER diffractometer, involving an X-ray source CuKα (λ = 1.5418 Å; acceleration potential = 45 kV; current = 200 mA); a Bragg-Brentano geometry was used.

The textural characteristics (surface area and porosity) were assessed by acquiring the corresponding nitrogen adsorption-desorption isotherms at 77 K, obtained with a Micromeritics TriStar II plus 2.02. The samples were previously outgassed for 12 h by heating up to 150 °C, under vacuum conditions.

2.4. Electrochemical analysis

The electrochemical tests were carried out in a conventional three-electrode compartment cell, in 0.1 mol dm^{-3} KOH electrolyte, using an Ag/AgCl (3 mol dm^{-3} KCl, Methrohm) reference electrode, a glassy carbon rod (diameter 2.0 mm, Metrohm) auxiliary electrode and a rotating disk electrode (RDE) of glassy carbon (diameter of 3.0 mm, Metrohm) as working electrode. An AutoLab PGSTAT 302N potensiostat/galvanostat controlled by Nova 2.1 software was used.

Prior to modification, the RDE was polished with diamond pastes (diameters of 6, 3 and 1 μm, MetaDi II, Buehler), using a microfiber polishing pad (BAS Bioanalytical Systems Inc.). The electrode was abundantly washed with ultrapure water and dried after each polishment. To prepare the catalyst ink, 1.0 mg of catalyst were dispersed in 20 μL Nafion 117 and 250 μL N,*N*-dimethylformamide, under ultrasonication for 20 min. The RDE was modified by drop-cast of 5.0 μL of the catalyst ink and dried under air flow.

The electrocatalytic activity towards ORR was analyzed by cyclic voltammetry (CV) and linear sweep voltammetry (LSV), in N_2- or O_2-saturated 0.1 mol dm^{-3} KOH electrolyte, at scan rate of 0.005 V s^{-1}. LSV measurements were carried out at different rotation speeds: 400, 800, 1200, 1600, 2000 and 3000 rpm. The currents obtained in O_2-saturated electrolyte were subtracted from the currents measured in N_2-saturated electrolyte to obtain the ORR currents.

The onset potential (E_{onset}) was determined as the potential at which the current density (j) reaches 5 % of the diffusion-limiting current density (j_L), in accordance with previously reported works [29]. ORR kinetics were evaluated through Koutecky-Levich (K-L) equation (eq. (1)) at several potentials:

$$\frac{1}{j}=\frac{1}{j_L}+\frac{1}{j_k}=\frac{1}{B\omega^{1/2}}+\frac{1}{j_k} \quad (1)$$

where j_k is the kinetic current density and ω is the angular velocity. B is calculated by eq. (2):

$$B = 0.2n_{O2}F(D_{O2})^{2/3}\nu^{-1/6}C_{O2} \quad (2)$$

where F stands for the Faraday constant (96.485C mol^{-1}), D_{O2} for the diffusion coefficient of O_2 ($1.95x10^{-5}$ cm^2 s^{-1}), ν for the kinematic viscosity of the electrolyte ($8.977x10^{-3}$ cm^2 s^{-1}) and C_{O2} for the bulk concentration of O_2 ($1.15x10^{-3}$ mol dm^{-3}); a constant of 0.2 was adopted for rotation speeds in rpm [28]. The number of electrons transferred per O_2 molecule (n_{O2}) was determined from the slope of K-L plots.

Tafel plots (E_{RHE} vs. log j_k) were obtained from LSV data corrected to diffusion (kinetic current). Mass transport corrections were performed using j_L. Kinetic current densities (j_k) were normalized by the mass of electrocatalysts loaded. Tafel slopes were calculated from eq. (3):

$$E - E^0 = a + b \log j_k \quad (3)$$

where E^0 is the standard potential, a is an exchange current density related constant and b is the Tafel slope.

The electrocatalyst stability was evaluated by chronoamperometry (CA) at $E = 0.45$ V vs. RHE and 1600 rpm for 54 000 s (15 h), in O_2-saturated 0.1 mol dm^{-3} KOH electrolyte.

All the potentials were measured *vs*. Ag/AgCl and then converted to the reversible hydrogen electrode (RHE), according to the Nernst equation (eq. (4)):

$$E_{RHE} = E_{Ag/AgCl} + 0.059pH + E^{\circ}_{Ag/AgCl} \quad (4)$$

where E_{RHE} and $E_{Ag/AgCl}$ stands for the potentials *vs*. RHE and Ag/AgCl scale, respectively, and $E^{\circ}_{Ag/AgCl} = 0.1976$ at 25 °C [30].

3. Results and discussion

3.1. Catalyst characterization

The morphology of the prepared materials was assessed by SEM (Fig. 1). The original biochar, CC, exhibited an extremely porous structure. The biochar doped with only N, N_6-CC, also presented some porosity, although with smaller pores than CC. On the other hand, the biochars co-doped with N and S (SN_6-CC, S_3N_3-CC and S_3N_2-CC) showed a distinct morphology, displaying severely wrinkled surfaces, while no pores could be observed.

The textural parameters of the prepared materials were assessed by N_2 adsorption-desorption isotherms at 77 K and can be consulted in Table 1. Among them, CC displayed the highest specific surface area (265.76 m^2 g^{-1}), followed by N_6-CC (256.07 m^2 g^{-1}), S_3N_2-CC (245.65 m^2 g^{-1}), SN_6-CC (222.66 m^2 g^{-1}) and S_3N_3-CC (180.16 m^2 g^{-1}). The same trend is verified for pore volume, with CC obtaining the highest volume (0.50 cm^3 g^{-1}) and S_3N_3-CC the lowest (0.29 cm^3 g^{-1}). On the other hand, regarding pore diameters, all the doped biochars presented similar values (6.52–6.66 nm), while CC exhibited wider pores with 7.57 nm. These results suggest that the doping procedure led to a decrease in surface area, but also in pore volume and diameter; this effect appeared to be more prominent in N and S co-doping than in N_6-CC. An even more significant decrease in surface area was previously reported after graphene doping *via* an analogous procedure and explained by the stacking of graphene sheets during the process [29].

The elemental composition of all materials was determined by CHNS (Table 2). All the prepared biochars were majorly composed of carbon, with carbon content between 69.81 % and 71.14 %, also containing a relatively similar content of hydrogen (0.75–0.85 %). However, the content of nitrogen and sulfur changed significantly after the doping procedure: the amount of nitrogen increased in all the doped biochars, while the content of sulfur reduced, compared to the undoped biochar. S_3N_3-CC displayed the largest amount of nitrogen (4.00 %), followed by N_6-CC (3.93 %), S_3N_2-CC (3.92 %), SN_6-CC (3.84) and CC (3.12 %). On the other hand, CC obtained the largest sulfur content (1.13 %), originated from the shrimp shells, while the biochar doped with S_3N_2, the dopant with highest S/N ratio, only achieved a content of 0.55 %; S_3N_3-CC showed an intermediate amount of sulfur (0.37 %), and SN_6-CC and

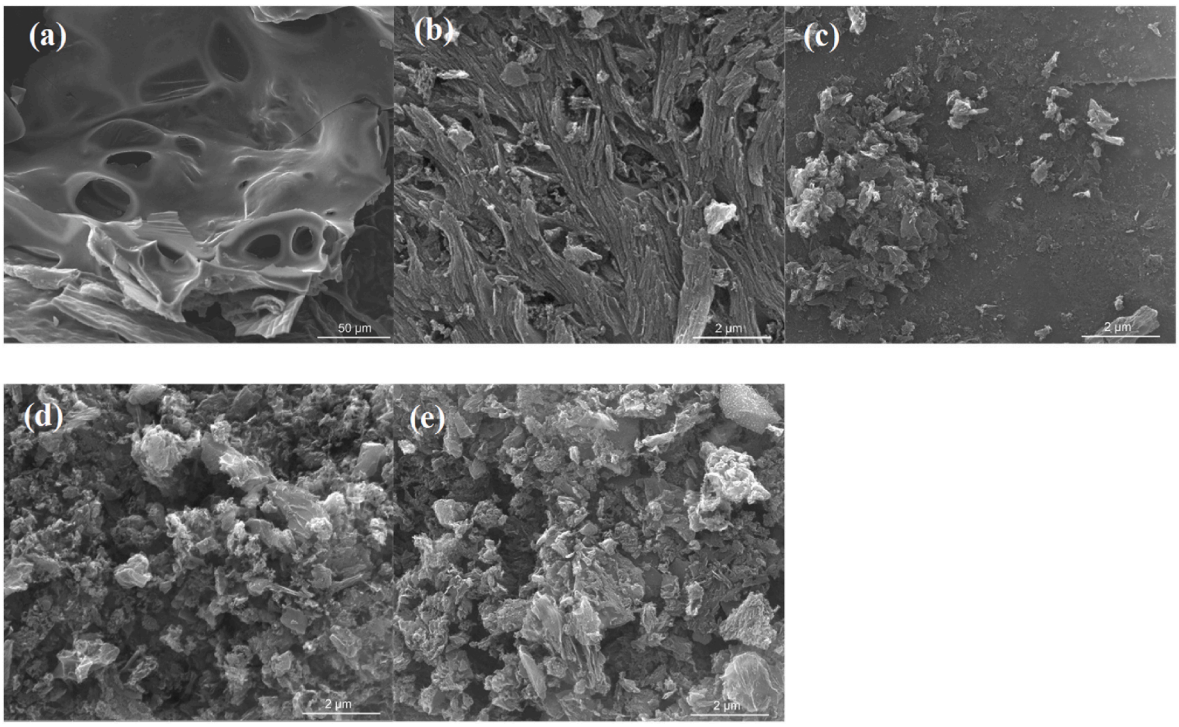

Fig. 1. – SEM micrographs of the prepared materials: (a) CC (1000 x), (b) N_6-CC (25000 x), (c) SN_6-CC (25000 x), (d) S_3N_3-CC (25000 x) and (e) S_3N_2-CC (25000 x).

Table 1
Textural parameters of the prepared materials determined by N_2 adsorption-desorption isotherms.

Catalyst	S_{BET} ($m^2\ g^{-1}$)	V_{pore} ($cm^3\ g^{-1}$)	D_{pore} (nm)
CC	265.76	0.50	7.57
N_6-CC	256.07	0.42	6.56
SN_6-CC	222.66	0.36	6.55
S_3N_3-CC	180.16	0.29	6.52
S_3N_2-CC	245.65	0.41	6.66

Table 2
Elemental analysis results for all the prepared materials.

Catalyst	% C	% N	% S	% H	% other
CC	71.00	3.12	1.13	0.85	23.91
N_6-CC	71.14	3.93	0.24	0.78	23.92
SN_6-CC	70.61	3.84	0.20	0.75	24.60
S_3N_3-CC	69.81	4.00	0.37	0.78	25.04
S_3N_2-CC	70.86	3.92	0.55	0.85	23.82

N_6-CC presented similar values (0.20 and 0.24 %, respectively). Therefore, the decrease in sulfur content in our doped biochars was related to the doping procedure, englobing both ball milling and a pyrolysis step, which may lead to the replacement of sulfur functionalities to nitrogen and/or oxygen functionalities.

Raman spectroscopy was used to determine the catalysts properties (Fig. 2 (a)). The D and G bands characteristic of carbon materials are observable in all spectra, around 1357.11–1362.15 cm^{-1} and 1582.88–1589.85 cm^{-1}, respectively (Table 3). Slightly shifts of the D band to lower Raman shift values were observed between CC and the doped biochars, while the G bands appeared at slightly higher Raman shift values after doping. This trend is often associated to an increase of the degree of structural order in carbon materials [31]. As the D band is assigned to conjugated sp^2 C domains and the G band is induced by phonon scattering at structural disorders in the carbon lattice, the intensity ratio of these bands (I_D/I_G) gives a measure of the structural defect density [32,33]. Herein, the intensities were obtained after fitting of D and G bands using Gaussian-Lorentzian functions. The I_D/I_G did not change between CC and N_6-CC (1.25 and 1.26, respectively), but decrease in SN_6-CC (1.09) and S_3N_3-CC (1.13), compared to the undoped biochar, indicating a higher graphitization degree and lower defect density of these materials. On the other hand, S_3N_2-CC showed an I_D/I_G of 1.33, which was slightly higher than the value of CC, suggesting the introduction of some structural defects. Nevertheless, all the doped biochars showed relatively close I_D/I_G values compared to CC (there was a maximum difference of 0.16), which indicates that the original crystalline structure of CC was mostly preserved during the doping approach.

The crystallinity of the prepared materials was evaluated by XRD (Fig. 2 (b)). It is possible to observe a broad peak around 25° in all spectra, corresponding to the diffraction plane (002) of graphitic materials [34,35]. The broadness of this peak suggests majorly amorphous materials, but with some crystalline structures, which is corroborated by the high I_D/I_G values obtained for all materials. Additionally, several low intensity peaks related to mineral phases (mainly $CaCO_3$ and CaO) originally present in shrimp shells can be detected between 30 and 52° in all spectra [36–38].

XPS analyses were performed to assess the atomic composition of all prepared materials, at a surface level. The distribution of elements can be consulted in Table 4. CC contained 90.55 % of carbon, 4.95 % of oxygen, 2.99 % of nitrogen, 1.01 % of sulfur and 0.50 % of phosphorus. The doped biochars also contained around 90 % of carbon (89.25, 89.61, 90.24 and 89.68 % for N_6-CC, SN_6-CC, S_3N_3-CC and S_3N_2-CC, respectively), but the oxygen content increased with the doping procedure (6.06–7.00 At %) in all doped biochars, except S_3N_3-CC, whose At % of oxygen decreased to 3.84. Nitrogen content increased in most doped biochars compared to CC, with S_3N_3-CC presenting the highest amount (4.02 %), followed by SN_6-CC (3.68 %) and N_6-CC (3.41 %), while S_3N_2-CC showed a similar nitrogen content to CC (2.87 %). On the other hand, the sulfur content decreased after doping in all biochars, as verified by CHNS: N_6-CC displayed the lowest sulfur amount at surface level (0.08 %), followed by SN_6-CC (0.22 %), S_3N_3-CC (0.37 %) and S_3N_2-CC (0.45 %). These results indicate that without the use a sulfur source during the doping approach there is an almost complete removal of the sulfur

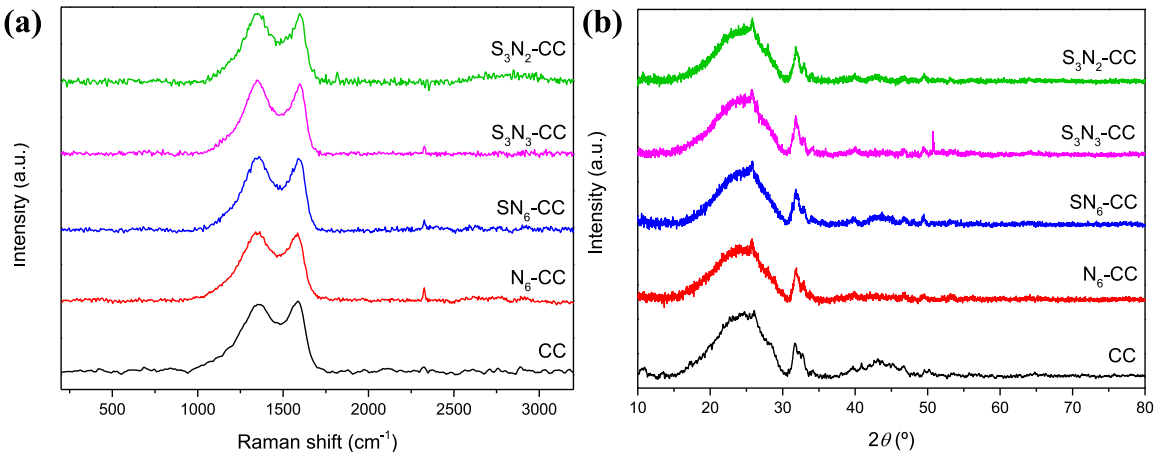

Fig. 2. – (a) Raman spectra and (b) diffractograms of the prepared materials.

Table 3
Raman shift associated to D and G bands, and I_D/I_G values obtained for all the prepared materials.

Catalyst	Raman shift (cm^{-1})		I_D/I_G
	D band	G band	
CC	1362.15	1582.88	1.25
N_6-CC	1357.11	1587.16	1.26
SN_6-CC	1358.70	1586.62	1.09
S_3N_3-CC	1357.40	1589.49	1.13
S_3N_2-CC	1357.85	1589.85	1.33

Table 4
– Surface atomic composition of the prepared catalysts determined by XPS.

Catalyst	At %					
	C 1s	O 1s	N 1s	S 2p	P 2p	Ca 2p
CC	90.55	4.95	2.99	1.01	0.50	–
N_6-CC	89.25	6.06	3.41	0.08	0.54	0.66
SN_6-CC	89.61	6.49	3.68	0.22	–	–
S_3N_3-CC	90.24	3.84	4.02	0.37	0.66	0.87
S_3N_2-CC	89.68	7.00	2.87	0.45	–	–

functionalities originally presented in CC at surface level , evidencing the importance of a careful dopant selection. Moreover, similar S incorporations were obtained in literature (0.2–0.3 At %) for graphene flakes doped with the same N and S precursors but associated to significantly lower N incorporation (1.2–2.6 At %) [39]. P 2p was only detected in CC, N_6-CC and S_3N_3-CC at At % of 0.50, 0.54 and 0.66 %, respectively, while Ca 2p was identified in N_6-CC (0.66 %) and S_3N_3-CC (0.87 %) but not in CC.

The high-resolution C 1s spectra of all prepared biochars were deconvoluted in six peaks, related to sp^2 carbon (284.60 eV), sp^3 carbon (285.20 eV), C–N (285.90 eV), C–O–C (286.90 eV), C=O (288.20 eV) and O–C=O (289.30 eV), plus a satellite peak associated to π–π* transitions (290.54–291.03 eV) (Fig. 3) [28,40]. Contributions from C–S/C=S should also be considered at 286–287 eV in all spectra [41], while C–O–P contributed to CC, N_6-CC and S_3N_3-CC C 1s spectra around 284–285 eV [42]. In all materials, the majority of carbon was under sp^2 C form, indicating the graphitic character of the prepared biochars.

High resolution N 1s spectra, represented in Fig. 4, were deconvoluted in four peaks, attributed to pyridinic N (398.15–398.33 eV), pyrrolic N (399.64–400.05 eV), graphitic N (400.97–401.30 eV) and oxidized N (402.31–403.90 eV) [23,43–45]. The content of each N form can be consulted in Table S1. While all the biochars presented majorly pyridinic N, its contents increased significantly after doping. The content of pyridinic N followed the trend CC (33.00 %) < N_6-CC (46.33 %) < S_3N_2-CC (46.50 %) < SN_6-CC (47.01 %) < S_3N_3-CC (50.87 %). On the other hand, the doping led to a considerable decrease in the content of pyrrolic N, following the trend S_3N_3-CC (16.65 %) < N_6-CC (22.58 %) < S_3N_2-CC (22.73 %) < SN_6-CC (24.46 %) < CC (32.67 %). Graphitic N increased slightly in S_3N_3-CC compared to CC but decreased in all the other doped biochars according to SN_6-CC (22.28 %) < S_3N_2-CC (23.08 %) < N_6-CC (24.34 %) < CC (26.33 %) < S_3N_3-CC (26.55 %). The doping approach did not alter significantly the content of oxidized N, although the doped biochars displayed slight smaller contents (5.96–7.69 %) than CC (8.00 %).

High resolution S 2p spectra of CC and N_6-CC were deconvoluted in three pairs of peaks corresponding to the $2p_{1/2}$ and $2p_{3/2}$ contribution of C–S–C (163.81–164.01 and 164.94–165.14, respectively), C–SH (165.38–165.89 and 166.52–167.02, respectively) and C–SO_2–C groups (167.92–167.94 and 169.05–169.07, respectively), plus a single peak at 169.69–170.11 eV attributed to C–SO_3 (Fig. 5(a) and (b)) [28,39]. Due to the lack of resolution, SN_6-CC spectrum was only deconvoluted in two main peaks at 164.18 and 165.38 eV related to S $2p_{3/2}$ and S $2p_{1/2}$ (Fig. 5 (c)), while S_3N_3-CC and S_3N_2-CC spectra displayed $2p_{3/2}$ and $2p_{1/2}$ contributions to C–S–C (164.03–164.11 and 165.16–165.24, respectively), C–SH (166.33–166.58 and 167.46–167.71, respectively) and C–SO_x–C groups (168.91–169.03 and 170.04–170.16, respectively) (Fig. 5(d) and (e)) [28,39]. Although is not possible to take considerations regarding SN_6-CC, the remaining biochars mainly contained thiophenic S, specially N_6-CC (72.99 %) and S_3N_3-CC (70.27 %), followed by CC (65.35 %) and S_3N_2-CC (57.78 %). The content of thiols increased after doping, from 10.89 % present in CC up to 22.22 % in S_3N_2-CC; N_6-CC and S_3N_3-CC showed intermediary amounts of 13.16 and 16.22 %, respectively.

Deconvoluted high resolution O 1s spectra of all prepared biochars can be found in Fig. S1. All spectra display three peaks corresponding to C=O, C–O and O–C=O groups around 530.90–531.08 eV, 531.99–532.44 eV and 533.60–533.98 eV, respectively [28,41]. N_6-CC and SN_6-CC spectra also show an extra band at 536.15 and 536.95 eV, respectively, related to adsorbed water at the catalyst surface [46].

Additionally, P 2p was detected in CC, N_6-CC and S_3N_3-CC (Fig. S2). CC spectrum was deconvoluted in three pairs of peaks, corresponding to $2p_{3/2}$ and $2p_{1/2}$ contributions of P–C (131.35 and 132.22 eV, respectively), $[P_2O_7]^{4-}$ (133.04 and 133.91 eV, respectively) and $[PO_3]^-$ (135.37 and 136.24 eV, respectively) [47]. On the other hand, N_6-CC and S_3N_3-CC spectra revealed only $2p_{3/2}$ and $2p_{1/2}$ contributions of $[P_2O_7]^{4-}$ (133.25–133.65 and 134.08–134.52 eV, respectively) and $[PO_3]^-$ (135.14–135.23 and 136.05–136.10 eV, respectively). Moreover, Ca 2p was detected only in N_6-CC and S_3N_3-CC (Fig. S3). Both spectra

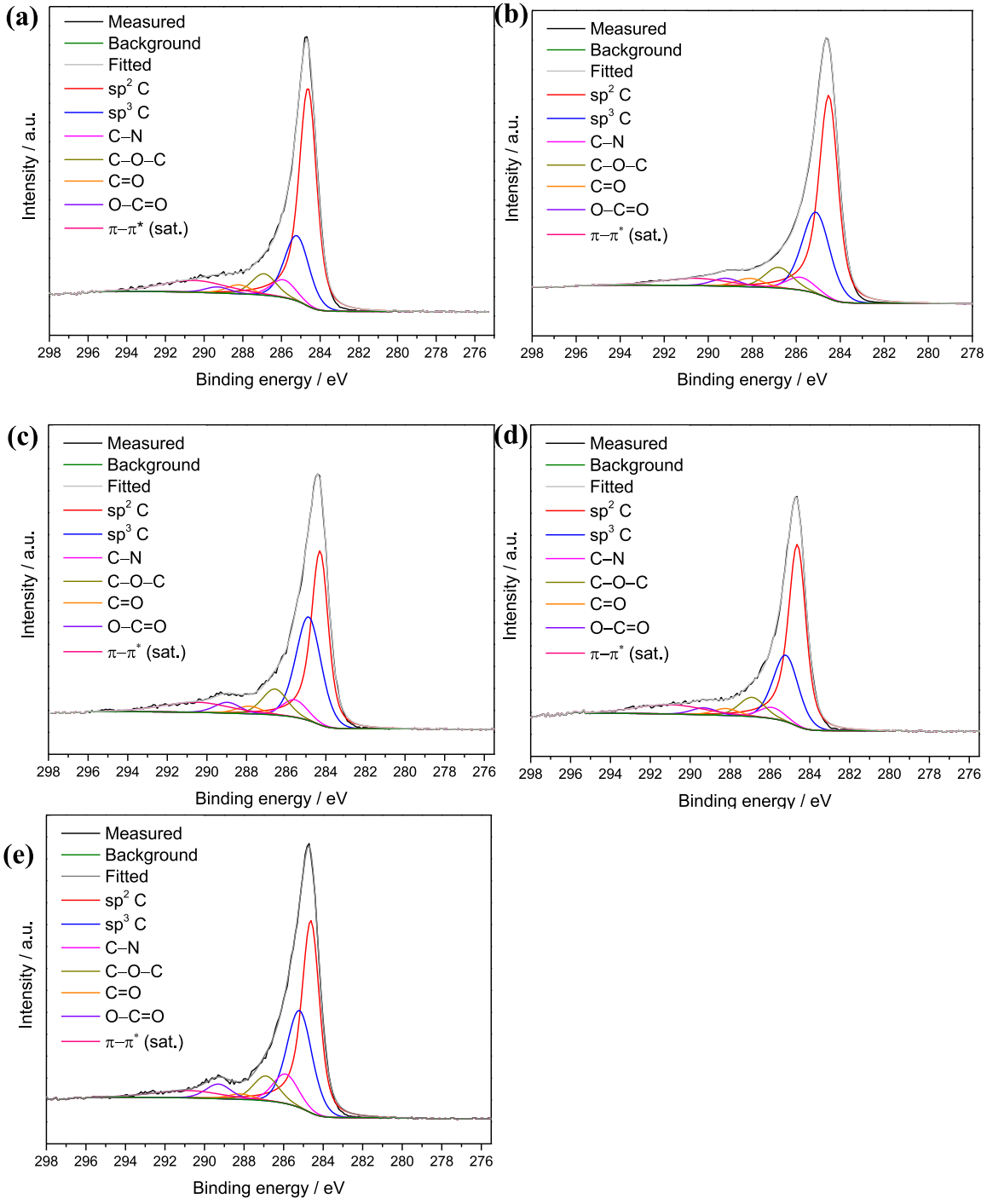

Fig. 3. – High resolution C 1s XPS spectra of (a) CC, (b) N_6-CC, (c) SN_6-CC, (d) S_3N_3-CC and (e) S_3N_2-CC.

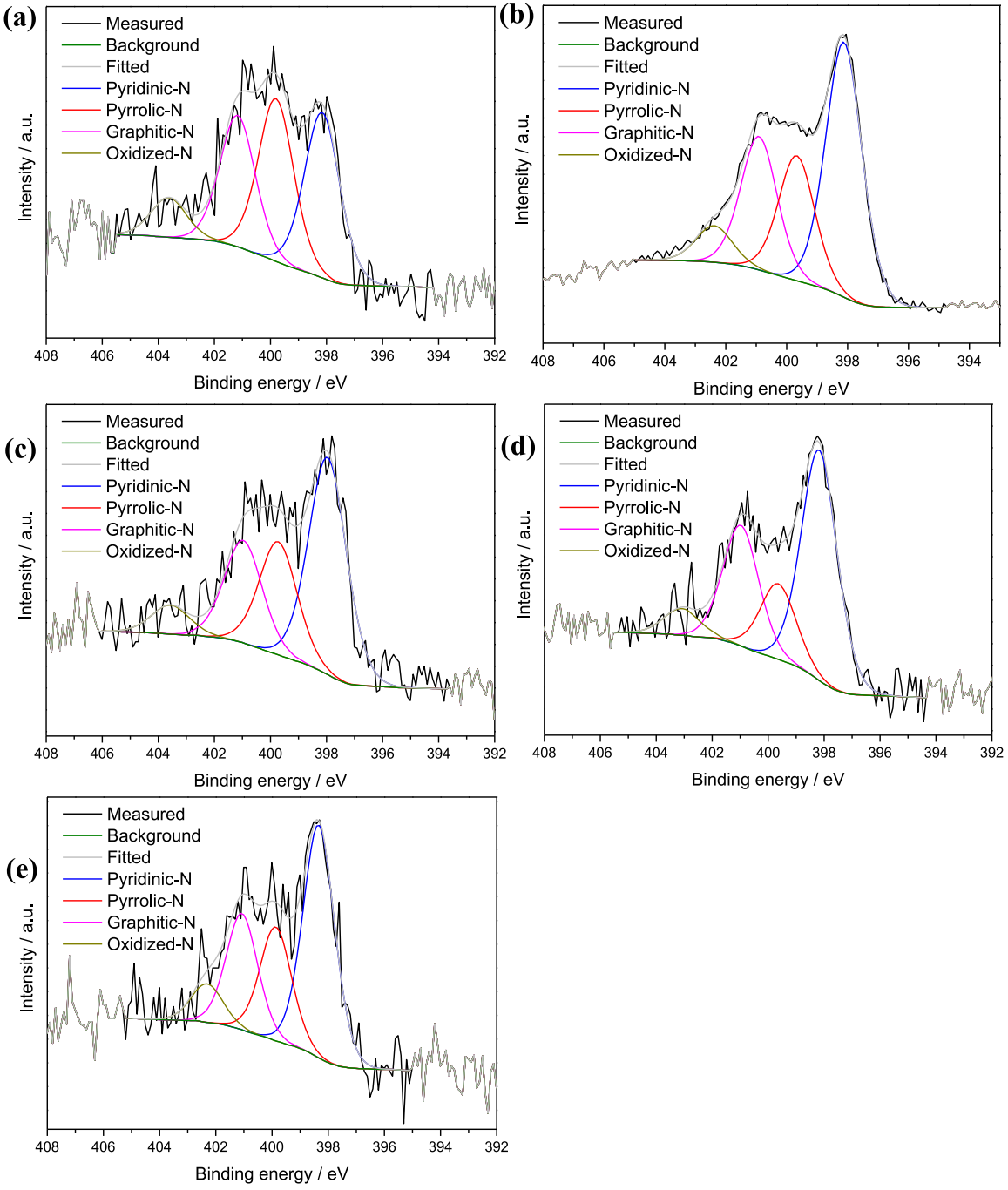

Fig. 4. – High resolution N 1s XPS spectra of (a) CC, (b) N_6-CC, (c) SN_6-CC, (d) S_3N_3-CC and (e) S_3N_2-CC.

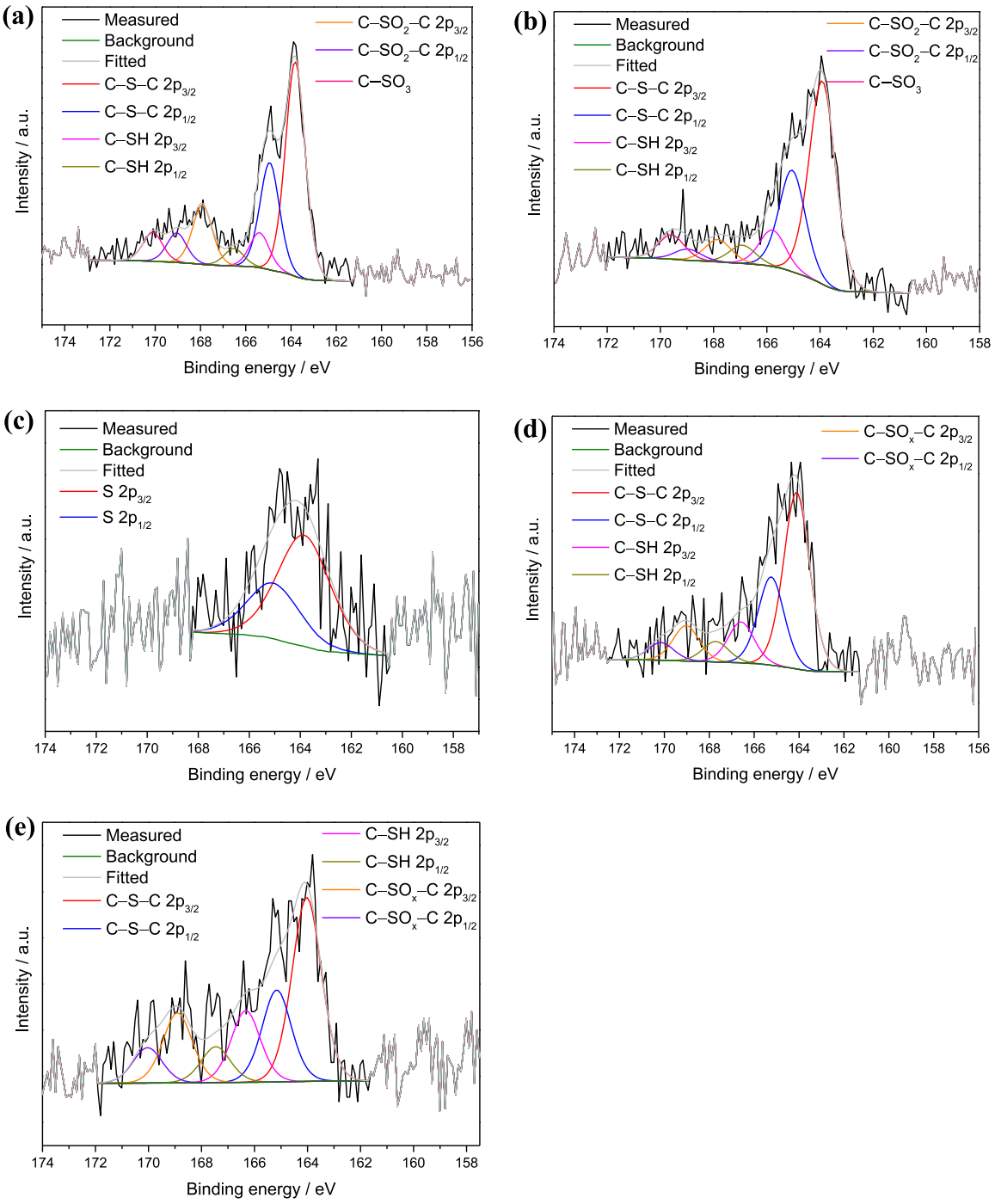

Fig. 5. – High resolution S 2p XPS spectra of (a) CC, (b) N_6-CC, (c) SN_6-CC, (d) S_3N_3-CC and (e) S_3N_2-CC.

presented a pair of peaks at 347.42–347.93 eV and 351.08–351.45 eV corresponding to $2p_{3/2}$ and $2p_{1/2}$ contributions of Ca in $CaCO_3$ [48,49].

3.2. Electrochemical characterization

The double-layer capacitance (C_{dl}) of the prepared materials was determined through a standard double-layer charging test, in which consecutive CVs were performed at several scan rates (20–160 mV s^{-1}), in N_2-saturated 0.1 mol dm^{-3} KOH solution (Fig. S4). C_{dl} values varied significantly in the prepared materials, with SN_6-CC showing the highest value (0.0067 mF cm^{-2}), followed by CC (0.0058 mF cm^{-2}), S_3N_3-CC (0.0046 mF cm^{-2}), N_6-CC (0.0045 mF cm^{-2}) and S_3N_2-CC (0.0033 mF cm^{-2}). For comparison, Pt/C obtained a C_{dl} of 0.0102 mF cm^{-2}.

The electrochemical surface area (ECSA) is related to double-layer capacitance by eq. (5):

$$\mathrm{ECSA} = \frac{C_{dl}}{C_{ref}} \quad (5)$$

in which C_{ref} represents a reference capacitance value per area unit [50]. Therefore, ECSA of the prepared materials followed the same trend presented by C_{dl}: SN_6-CC > CC > S_3N_3-CC > N_6-CC > S_3N_2-CC. However, as reported C_{ref} values for complex materials, such as biochars, are often unreliable, ECSA values were not determined.

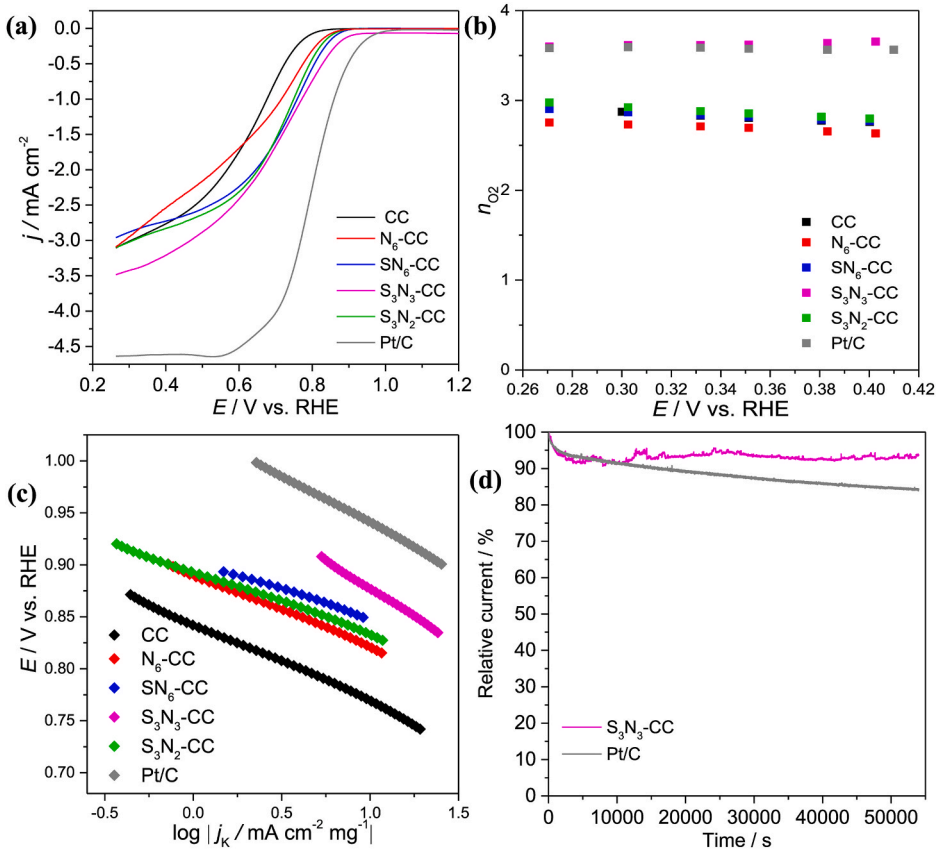

Fig. 6. – ORR performance of all prepared electrocatalysts plus Pt/C: (a) ORR polarization curves in O_2-saturated 0.1 mol dm^{-3} KOH, at 1600 rpm and 0.005 mV s^{-1}, (b) evolution of n_{O2} at different potentials, (c) Tafel plots and (d) chronoamperograms at $E = 0.45$ V vs. RHE for S_3N_3-CC and Pt/C in O_2-saturated 0.1 mol dm^{-3} KOH, at 1600 rpm and 0.005 V s^{-1}.

3.3. ORR results

The ORR performance of all prepared materials was first evaluated by cyclic voltammetry in N_2 and O_2-saturated 0.1 mol dm^{-3} KOH. The resulting CVs can be found in Fig. S5. As expected, the CVs of the doped and undoped biochars show no electrochemical processes in N_2-saturated electrolyte, while Pt/C displayed cathodic and anodic peaks related to redox processes of platinum. However, in O_2-saturated electrolyte a cathodic peak appears around 0.72, 0.77, 0.79, 0.79, 0.77 and 0.86 V vs. RHE in CC, N_6-CC, SN_6-CC, S_3N_3-CC, S_3N_2-CC and Pt/C CV's, respectively, corresponding to the oxygen reduction.

The electrocatalytic behavior of the prepared biochars was further evaluated by linear sweep voltammetry. The LSVs obtained in O_2-saturated 0.1 mol dm^{-3} KOH, at 1600 rpm, are represented in Fig. 6 (a). S_3N_3-CC achieved the most positive E_{onset} of the catalyst series (0.88 V vs. RHE), followed by SN_6-CC (0.85 V vs. RHE), S_3N_2-CC (0.84 V vs. RHE), N_6-CC (0.83 V vs. RHE) and CC (0.78 V vs. RHE); by comparison, Pt/C obtained an E_{onset} of 0.93 V vs. RHE (Table 5). S_3N_3-CC also displayed the highest diffusion-limiting current density (j_L), at −3.49 mA cm^{-2}, while the remaining catalysts showed considerably lower values: 3.11 mA cm^{-2} for CC and S_3N_2-CC, −3.09 mA cm^{-2} for N_6-CC and −2.95 mA cm^{-2} for SN_6-CC (Table 5). Meanwhile, Pt/C obtained j_L of −4.62 mA cm^{-2}. These results suggest that (*i*) biochar doping is fundamental for obtain more positive E_{onset}; (*ii*) N,S co-doping led to enhanced E_{onset} compared to N doping, possibly due to a combination of the charge density redistribution on the biochar surface, induced by the presence of more electronegative N atoms (compared to C and S), and the introduction of S–C bonds that led to polarization of spin distribution of C atoms [16,51]; (*iii*) the selection of the dopants has a strong effect in j_L, as only S_3N_3-CC achieved a higher value than the undoped CC. Moreover, the sum of pyridinic and graphitic N ($N_{pyridinic} + N_{graphitic}$), as well as the ratio between pyridinic and pyrrolic N ($N_{pyridinic}/N_{pyrrolic}$), seemed to be related to the E_{onset} in the prepared biochars, with an increase of both $N_{pyridinic} + N_{graphitic}$ and $N_{pyridinic}/N_{pyrrolic}$ values leading to more positive E_{onset}, as observed in Fig. S6.

Table 5
ORR performance of the prepared electrocatalysts and Pt/C.

Catalyst	E_{onset}/V vs. RHE	j_L/mA cm^{-2}	n_{O2}	Tafel slope/mV dec^{-1}
CC	0.78	−3.11	2.83	74
N_6-CC	0.83	−3.09	2.70	68
SN_6-CC	0.85	−2.95	2.85	56
S_3N_3-CC	0.88	−3.49	3.62	107
S_3N_2-CC	0.84	−3.11	2.88	59
Pt/C	0.93	−4.62	3.58	91

It is worth to mention that the most promising electrocatalyst, S_3N_3-CC, obtained similar E_{onset} and j_L values compared to other heteroatom doped biochars reported in literature, as can be consulted in Table S2. Moreover, it also displayed very similar values compared to graphene doped with S_3N_3 prepared by the same procedure here described, previously reported by our group ($E_{onset} = 0.84$ V vs. RHE and $j_L = -3.49$ mA cm^{-2}) [28], indicating that our shrimp shell-derived biochar is able to compete with commercial carbon nanomaterials.

The ORR kinetics of the prepared materials was investigated through K-L plots, constructed using LSVs measurements at different rotation speeds, namely 400, 800, 1200, 1600, 2000 and 3000 rpm (Fig. S7). As all the plots showed a good linear correlation between $1/j$ and $\omega^{-0.5}$, the reaction followed a first order kinetic regarding the dissolved O_2 concentration [52]. Fig. 6 (b) shows the evolution of the number of electrons involved in ORR process per O_2 molecule (n_{O2}) at different

potentials; n_{O2} values were estimated using K-L plots at several potentials. S_3N_3-CC and Pt/C displayed nearly constant n_{O2} values over the selected potential window, while the remaining catalysts showed decreasing n_{O2} at more positive potentials, indicating the mechanism dependency of the applied potential in these catalysts. S_3N_3-CC obtained the average n_{O2} closer to 4 (3.62), comparable to Pt/C (3.58) as it can observed in Table 5. On the other hand, the remaining catalysts presented values closer to 3, namely 2.83, 2.70, 2.85 and 2.88 for CC, N_6-CC, SN_6-CC and S_3N_2-CC, respectively, indicating a mixed process between the 2 and 4 electron reduction. As occurred with j_L, the selectivity for the 2 or 4 electron pathway seems to be greatly influenced by the choice of N and/or S source, with the biochar doped with S_3N_3 obtaining the most promising results but the other doped biochars obtaining similar or even worse results than CC. While the nature of ORR active sites in heteroatom doped carbon materials is still not consensual [17,51,53], most researchers consider that pyridinic and graphitic N are the main drivers for the 4-electron reduction [17,54]. This study corroborates that hypothesis, as S_3N_3-CC showed the closest n_{O2} to 4 and also the highest amount of both pyridinic and graphitic N relatively to the remaining doped biochars. However, compared to the undoped CC, the other doped biochars also presented higher content of pyridinic N, but lower percentage of graphitic N, suggesting that graphitic N displayed a very important role in determining the selectivity for the 4-electron pathway. Nevertheless, it should be considered that other factors, including the S content and S functionalities or the presence of P in some biochars, may also be influencing the number of electrons involved in the process.

The Tafel slopes (TS) of the prepared materials were determined from Tafel plots (Fig. 6 (c)). TS values can be found in Table 5. In the analyzed potential window, CC, N_6-CC, SN_6-CC, S_3N_3-CC and S_3N_2-CC displayed TS of 74, 68, 56, 107 and 59 mV dec^{-1}, respectively; for comparison, Pt/C obtained TS of 91 mV dec^{-1}. These values suggest that all the prepared materials follow a similar ORR mechanism, with the overall reaction rate described by eq. (6), where M is an empty site on the catalyst surface [55].

$$MO_2^- + H_2O \rightleftharpoons MO_2H + OH^- \quad (6)$$

The performance of the most promising catalyst (S_3N_3-CC) was also evaluated by chronoamperometry at $E = 0.45$ V vs. RHE over 15 h, in order to verify its ability to retain a stable current density at a fixed potential over time and compared with Pt/C (Fig. 6 (d)). S_3N_3-CC showed excellent current density stability, with a current retention of 94 %, even outperforming Pt/C, with retention of only 84 %.

Overall, S_3N_3-CC displayed excellent ORR performance, even comparable to Pt/C in terms of selectivity for the 4-electron reduction and outperforming it in terms of stability, although some improvement is still needed to increase j_L and lower the overpotential. These outstanding results were tentatively attributed to (*i*) a high amount of pyridinic and graphitic N, the main active sites in N-doped carbons; (*ii*) the introduction of thiophene-S, which are considered the main ORR active site in S-doped carbons [16,19]; and (*iii*) an optimized N/S ratio that led to enhanced charge and spin density distribution on the biochar surface, promoting the ORR process. However, our doped biochars differed significantly from each other, presenting different surface area, ECSA, morphology and chemical composition. Therefore, it is complex to fully explain their electrocatalytic behavior as some additional factors, besides the introduction of certain N and S functionalities, may have contributed to S_3N_3-CC enhanced performance.

4. Conclusions

Several heteroatom doped biochars, derived from shrimp shells, were prepared through a three-step procedure, involving an initial pyrolysis to obtain the biochar CC, followed by mixing with S and/or N precursors *via* solventless ball milling and a second pyrolysis step. Four distinct dopants were tested, namely N_6, SN_6, S_3N_3 and S_3N_2. The resulting materials were extensively characterized by several techniques (elemental analysis, SEM, N_2 adsorption/desorption isotherms, Raman, XRD and XPS) and their ORR performance was evaluated in alkaline medium.

Overall, both N doping and N and S co-doping led to enhanced electrocatalytic results. S_3N_3-CC achieved the most promising ORR activity, obtaining an E_{onset} of 0.88 V vs. RHE, j_L of -3.49 mA cm^{-2} and n_{O2} of 3.62, which represented an increase of 100 mV and 0.38 mA cm^{-2} in E_{onset} and j_L, respectively, compared to the initial biochar CC, besides the shift from CC's mixed ORR mechanism ($n_{O2} = 2.83$) to a mostly 4 electron process. Moreover, S_3N_3-CC displayed an excellent stability, with current retention around 94 % at 15 h of use. S_3N_3-CC performance was mainly attributed to the larger content of pyridinic and graphitic N, as well as the higher ratio between pyridinic and pyrrolic N, in relation to the other prepared biochars. Meanwhile, the presence of thiophenic S in S_3N_3-CC also favored the ORR process. Although S_3N_3-CC still underperformed commercial Pt/C in some parameters, it should be considered that our biochar is completely metal free and obtained through sustainable processes, contributing to the development of cost-effective ORR electrocatalysts.

CRediT authorship contribution statement

Renata Matos: Writing – original draft, Investigation, Formal analysis. **António J.S. Fernandes:** Investigation. **Victor K. Abdelkader-Fernández:** Investigation. **Andreia F. Peixoto:** Writing – review & editing, Project administration, Funding acquisition, Conceptualization. **Diana M. Fernandes:** Writing – review & editing, Supervision, Funding acquisition, Conceptualization.

Acknowledgements

This work was funded by Portuguese funds through Fundação para a Ciência e a Tecnologia (FCT/MCTES) in the framework of the project EXPL/BII-BIO/0436/2021. Thanks are also due to FCT for Laboratório Associado para a Química Verde - Tecnologias e Processos Limpos funding: 10.54499/LA/P/0008/2020, 10.54499/UIDP/50006/2020 and 10.54499/UIDB/50006/2020. D.M.F. and A.F.P. thank FCT for funding through the Individual Call to Scientific Employment Stimulus (Refs. 2021.00771.CEECIND/CP1662/CT0007 (10.54499/2021.00771.CEECIND/CP1662/CT0007) and 2020.01614.CEECIND/CP1596/CT0007 (10.54499/2020.01614.CEECIND/CP1596/CT0007) respectively). RM thanks FCT the PhD fellowship 2020.05342.BD (10.54499/2020.05342.BD). VKAF thanks the Junta de Andalucía (Spanish regional government) for his current Postdoc contract (PAIDI 2020, Young Doctors Program).

Appendix A. Supplementary data

Supplementary data to this article can be found online at https://doi.org/10.1016/j.biombioe.2024.107523.

Data availability

Data will be made available on request.

References

[1] L.X. Fan, Z.K. Tu, S.H. Chan, Recent development of hydrogen and fuel cell technologies: a review, Energy Rep. 7 (2021) 8421–8446.
[2] Q.F. Liu, Z.F. Pan, E.D. Wang, L. An, G.Q. Sun, Aqueous metal-air batteries: fundamentals and applications, Energy Storage Mater. 27 (2020) 478–505.
[3] C. Freire, D.M. Fernandes, M. Nunes, V.K. Abdelkader, POM & MOF-based electrocatalysts for energy-related reactions, ChemCatChem 10 (8) (2018) 1703–1730.
[4] J. Stacy, Y.N. Regmi, B. Leonard, M.H. Fan, The recent progress and future of oxygen reduction reaction catalysis: a review, Renew. Sustain. Energy Rev. 69 (2017) 401–414.

[5] L.T. Qu, Y. Liu, J.B. Baek, L.M. Dai, Nitrogen-doped graphene as efficient metal-free electrocatalyst for oxygen reduction in fuel cells, ACS Nano 4 (3) (2010) 1321–1326.

[6] D.S. Yang, D. Bhattacharjya, M.Y. Song, J.S. Yu, Highly efficient metal-free phosphorus-doped platelet ordered mesoporous carbon for electrocatalytic oxygen reduction, Carbon 67 (2014) 736–743.

[7] X. Feng, Y. Bai, M.Q. Liu, Y. Li, H.Y. Yang, X.R. Wang, C. Wu, Untangling the respective effects of heteroatom-doped carbon materials in batteries, supercapacitors and the ORR to design high performance materials, Energy Environ. Sci. 14 (4) (2021) 2036–2089.

[8] H. Wang, X.J. Bo, Y.F. Zhang, L.P. Guo, Sulfur-doped ordered mesoporous carbon with high electrocatalytic activity for oxygen reduction, Electrochim. Acta 108 (2013) 404–411.

[9] K.P. Gong, F. Du, Z.H. Xia, M. Durstock, L.M. Dai, Nitrogen-doped carbon nanotube arrays with high electrocatalytic activity for oxygen reduction, Science 323 (5915) (2009) 760–764.

[10] Z. Yang, Z. Yao, G.F. Li, G.Y. Fang, H.G. Nie, Z. Liu, X.M. Zhou, X. Chen, S. M. Huang, Sulfur-doped graphene as an efficient metal-free cathode catalyst for oxygen reduction, ACS Nano 6 (1) (2012) 205–211.

[11] Z.W. Liu, F. Peng, H.J. Wang, H. Yu, W.X. Zheng, J.A. Yang, Phosphorus-doped graphite layers with high electrocatalytic activity for the O_2 reduction in an alkaline medium, Angew. Chem.-Int. Edit. 50 (14) (2011) 3257–3261.

[12] G. Panomsuwan, N. Saito, T. Ishizaki, Simple one-step synthesis of fluorine-doped carbon nanoparticles as potential alternative metal-free electrocatalysts for oxygen reduction reaction, J. Mater. Chem. A 3 (18) (2015) 9972–9981.

[13] X.J. Sun, Y.W. Zhang, P. Song, J. Pan, L. Zhuang, W.L. Xu, W. Xing, Fluorine-doped carbon blacks: highly efficient metal-free electrocatalysts for oxygen reduction reaction, ACS Catal. 3 (8) (2013) 1726–1729.

[14] X.J. Bo, L.P. Guo, Ordered mesoporous boron-doped carbons as metal-free electrocatalysts for the oxygen reduction reaction in alkaline solution, Phys. Chem. Chem. Phys. 15 (7) (2013) 2459–2465.

[15] A.R. Jang, Y.W. Lee, S.S. Lee, J. Hong, S.H. Beak, S. Pak, J. Lee, H.S. Shin, D. Ahn, W.K. Hong, S. Cha, J.I. Sohn, I.K. Park, Electrochemical and electrocatalytic reaction characteristics of boron-incorporated graphene *via* a simple spin-on dopant process, J. Mater. Chem. A 6 (17) (2018) 7351–7356.

[16] T.T. Jiang, Y. Wang, K. Wang, Y.R. Liang, D.C. Wu, P. Tsiakaras, S.Q. Song, A novel sulfur-nitrogen dual doped ordered mesoporous carbon electrocatalyst for efficient oxygen reduction reaction, Appl. Catal. B Environ. 189 (2016) 1–11.

[17] J. Quílez-Bermejo, E. Morallón, D. Cazorla-Amorós, Metal-free heteroatom-doped carbon-based catalysts for ORR: a critical assessment about the role of heteroatoms, Carbon 165 (2020) 434–454.

[18] J. Liang, Y. Jiao, M. Jaroniec, S.Z. Qiao, Sulfur and nitrogen dual-doped mesoporous graphene electrocatalyst for oxygen reduction with synergistically enhanced performance, Angew. Chem.-Int. Edit. 51 (46) (2012) 11496–11500.

[19] Y.F. Li, M. Li, L.Q. Jiang, L. Lin, L.L. Cui, X.Q. He, Advanced oxygen reduction reaction catalyst based on nitrogen and sulfur co-doped graphene in alkaline medium, Phys. Chem. Chem. Phys. 16 (42) (2014) 23196–23205.

[20] S.B. Patwardhan, S. Pandit, P.K. Gupta, N.K. Jha, J. Rawat, H.C. Joshi, K. Priya, M. Gupta, D. Lahiri, M. Nag, V.K. Thakur, K.K. Kesari, Recent advances in the application of biochar in microbial electrochemical cells, Fuel 311 (2022) 16.

[21] R. Ramos, V.K. Abdelkader-Fernandez, R. Matos, A.F. Peixoto, D.M. Fernandes, Metal-Supported biochar catalysts for sustainable biorefinery, electrocatalysis, and energy storage applications: a review, Catal. 12 (2) (2022) 66.

[22] Z.Y. Fan, J. Li, W. Yang, Q. Fu, K. Sun, Y.C. Song, Z.D. Wei, Q. Liao, X. Zhu, Green and facile synthesis of iron oxide nanoparticle-embedded N-doped biocarbon as an efficient oxygen reduction electrocatalyst for microbial fuel cells, Chem. Eng. J. 385 (2020) 10.

[23] Y. Ding, S.Q. Huang, Y.K. Sun, Y.C. Li, L.J. Zhu, S.R. Wang, Preparation of nitrogen and sulfur Co-doped and interconnected hierarchical porous biochar by pyrolysis of Mantis shrimp in CO_2 atmosphere for symmetric supercapacitors, Chemelectrochem 8 (19) (2021) 3745–3754.

[24] B.P. Qiu, X. Wei, W. Zhang, Y.H. Lv, H.L. Meng, F. Wei, Shrimp shell-derived N, O-doped honeycomb-carbon for high-performance supercapacitor, Diam. Relat. Mater. 136 (2023) 9.

[25] F. Gao, J.Y. Qu, C. Geng, G.H. Shao, M.B. Wu, Self-templating synthesis of nitrogen-decorated hierarchical porous carbon from shrimp shell for supercapacitors, J. Mater. Chem. A 4 (19) (2016) 7445–7452.

[26] H. Amiri, M. Aghbashlo, M. Sharma, J. Gaffey, L. Manning, S.M.M. Basri, J. F. Kennedy, V.K. Gupta, M. Tabatabaei, Chitin and chitosan derived from crustacean waste valorization streams can support food systems and the UN Sustainable Development Goals, Nat. Food 3 (10) (2022) 822–828.

[27] N. Yan, X. Chen, Don't waste seafood waste, Nat. 524 (7564) (2015) 155–157.

[28] D.M. Fernandes, P. Mathumba, A.J.S. Fernandes, E.I. Iwuoha, C. Freire, Towards efficient oxygen reduction reaction electrocatalysts through graphene doping, Electrochim. Acta 319 (2019) 72–81.

[29] M. Nunes, D.M. Fernandes, M.V. Morales, I. Rodríguez-Ramos, A. Guerrero-Ruiz, C. Freire, Cu-based N-doped/undoped graphene nanocomposites as electrocatalysts for the oxygen reduction, J. Appl. Electrochem. 49 (7) (2019) 693–703.

[30] S. Hoang, S.W. Guo, N.T. Hahn, A.J. Bard, C.B. Mullins, Visible light driven photoelectrochemical water oxidation on nitrogen-modified TiO_2 nanowires, Nano Lett. 12 (1) (2012) 26–32.

[31] J. Xu, J.W. Liu, P. Ling, X. Zhang, K. Xu, L.M. He, Y. Wang, S. Su, S. Hu, J. Xiang, Raman spectroscopy of biochar from the pyrolysis of three typical Chinese biomasses: a novel method for rapidly evaluating the biochar property, Energy 202 (2020) 10.

[32] L.M. Malard, M.A. Pimenta, G. Dresselhaus, M.S. Dresselhaus, Raman spectroscopy in graphene, Phys. Rep.-Rev. Sec. Phys. Lett. 473 (5–6) (2009) 51–87.

[33] D. Kumbhar, A. Palliyarayil, D. Reghu, D. Shrungar, S. Umapathy, S. Sil, Rapid discrimination of porous bio-carbon derived from nitrogen rich biomass using Raman spectroscopy and artificial intelligence methods, Carbon 178 (2021) 792–802.

[34] K. Li, Q.F. Liu, H.F. Cheng, M.S. Hu, S. Zhang, Classification and carbon structural transformation from anthracite to natural coaly graphite by XRD, Raman spectroscopy, and HRTEM, Spectroc. Acta Pt. A-Molec. Biomolec. Spectr. 249 (2021) 10.

[35] Z.Q. Li, C.J. Lu, Z.P. Xia, Y. Zhou, Z. Luo, X-ray diffraction patterns of graphite and turbostratic carbon, Carbon 45 (8) (2007) 1686–1695.

[36] J. Liu, X.Y. Yang, H.H. Liu, X.P. Jia, Y.C. Bao, Mixed biochar obtained by the co-pyrolysis of shrimp shell with corn straw: Co-pyrolysis characteristics and its adsorption capability, Chemosphere 282 (2021) 13.

[37] M.C. Reis, M.F.B. Sousa, F. Alobaid, C.A. Bertran, Y. Wang, A two-fluid model for calcium carbonate precipitation in highly supersaturated solutions, Adv. Powder Technol. 29 (7) (2018) 1571–1581.

[38] O.P. Gbenebor, S.O. Adeosun, G.I. Lawal, S. Jun, S.A. Olaleye, Acetylation, crystalline and morphological properties of structural polysaccharide from shrimp exoskeleton, Eng. Sci. Technol. 20 (3) (2017) 1155–1165.

[39] R. Braga, D.M. Fernandes, A. Adán-Más, T.M. Silva, M.F. Montemor, The role of the precursor on the electrochemical performance of N,S Co-doped graphene electrodes in aqueous electrolytes, Batter. -Basel 9 (3) (2023) 19.

[40] I.S. Marques, B. Jarrais, R. Ramos, V.K. Abdelkader-Fernandez, A. Yaremchenko, C. Freire, D.M. Fernandes, A.F. Peixoto, Nitrogen-doped biochar-supported metal catalysts: high efficiency in both catalytic transfer hydrogenation of furfural and electrocatalytic oxygen reactions, Catal. Today 418 (2023) 13.

[41] R. Matos, M.S. Nunes, I. Kuzniarska-Biernacka, M. Rocha, A. Guedes, A.C. Estrada, J.L. Lopes, T. Trindade, C. Freire, Graphene@Metal sulfide/oxide nanocomposites as novel photo-fenton-like catalysts for 4-nitrophenol degradation, Eur. J. Inorg. Chem. 2021 (47) (2021) 4915–4928.

[42] A.M. Puziy, O.I. Poddubnaya, R.P. Socha, J. Gurgul, M. Wisniewski, XPS and NMR studies of phosphoric acid activated carbons, Carbon 46 (15) (2008) 2113–2123.

[43] B. Jarrais, A. Guedes, C. Freire, Heteroatom-doped carbon nanomaterials as metal-free catalysts for the reduction of 4-nitrophenol, ChemistrySelect 3 (6) (2018) 1737–1748.

[44] D.H. Wu, H. Huang, M. Ul Haq, L. Zhang, J.J. Feng, A.J. Wang, Lignin-derived iron carbide/Mn, N, S-codoped carbon nanotubes as a high-efficiency catalyst for synergistically enhanced oxygen reduction reaction and rechargeable zinc-air battery, J. Colloid Interfac. Sci. 647 (2023) 1–11.

[45] H.L. Meng, S.Y. Lin, J.J. Feng, L. Zhang, A.J. Wang, Coordination regulated pyrolysis synthesis of ultrafine FeNi/$(FeNi)_9S_8$ nanoclusters/nitrogen, sulfur-codoped graphitic carbon nanosheets as efficient bifunctional oxygen electrocatalysts, J. Colloid Interfac. Sci. 610 (2022) 573–582.

[46] B. Jarrais, A. Guedes, C. Freire, Selectively oxidized carbon nanocatalysts for the oxidation of *cis*-cyclooctene, New J. Chem. 42 (3) (2018) 2306–2319.

[47] Y.Y. Wen, B. Wang, C.C. Huang, L.Z. Wang, D. Hulicova-Jurcakova, Synthesis of phosphorus-doped graphene and its wide potential window in aqueous supercapacitors, Chem.-Eur. J. 21 (1) (2015) 80–85.

[48] C.S. Gopinath, S.G. Hegde, A.V. Ramaswamy, S. Mahapatra, Photoernission studies of polymorphic $CaCO_3$ materials, Mater. Res. Bull. 37 (7) (2002) 1323–1332.

[49] J.F. Moulder, J. Chastain, Handbook of X-Ray Photoelectron Spectroscopy: A Reference Book of Standard Spectra for Identification and Interpretation of XPS Data, Physical Electronics Division, Perkin-Elmer Corporation, 1992.

[50] I.S. Marques, B. Jarrais, I.M. Mbomekallé, A.L. Teillout, P. de Oliveira, C. Freire, D. M. Fernandes, Synergetic effects of mixed-metal Polyoxometalates@Carbon-based composites as electrocatalysts for the oxygen reduction and the oxygen evolution reactions, Catal. 12 (4) (2022) 14.

[51] N. Yang, L. Li, J. Li, W. Ding, Z.D. Wei, Modulating the oxygen reduction activity of heteroatom-doped carbon catalysts via the triple effect: charge, spin density and ligand effect, Chem. Sci. 9 (26) (2018) 5795–5804.

[52] D.M. Fernandes, H.C. Novais, R. Bacsa, P. Serp, B. Bachiller-Baeza, I. Rodríguez-Ramos, A. Guerrero-Ruiz, C. Freire, Polyoxotungstate@Carbon nanocomposites as oxygen reduction reaction (ORR) electrocatalysts, Langmuir 34 (22) (2018) 6376–6387.

[53] J.C. Li, X.P. Qin, P.X. Hou, M. Cheng, C. Shi, C. Liu, H.M. Cheng, M.H. Shao, Identification of active sites in nitrogen and sulfur co-doped carbon-based oxygen reduction catalysts, Carbon 147 (2019) 303–311.

[54] I.M. Rocha, O. Soares, D.M. Fernandes, C. Freire, J.L. Figueiredo, M.F.R. Pereira, N-Doped carbon nanotubes for the oxygen reduction reaction in alkaline medium: synergistic relationship between pyridinic and quaternary nitrogen, ChemistrySelect 1 (10) (2016) 2522–2530.

[55] T. Shinagawa, A.T. Garcia-Esparza, K. Takanabe, Insight on Tafel slopes from a microkinetic analysis of aqueous electrocatalysis for energy conversion, Sci. Rep. 5 (2015) 21.